

Influence of Grain Size on the Electrochemical Performance of $\text{Li}_{7-3x}\text{La}_3\text{Zr}_2\text{Al}_x\text{O}_{12}$ Solid Electrolyte

Miriam Botros,^{*[a]} Jesus Gonzalez-Julian,^[b, c] Torsten Scherer,^[a, h] Radian Popescu,^[d] Christoph Loho,^[e, g] Askar Kilmametov,^[a] Oliver Clemens,^[f] and Horst Hahn^[a, g, i]

Contemporary Li-ion batteries are facing substantial challenges like safety and limited energy density. The development of all-solid-state battery cells mitigates safety hazards and allows the use of Li-metal anodes increasing energy density. Garnet-type solid electrolytes can be vital to achieving an all-solid-state cell and an understanding of the influence of its microstructure on the electrochemical performance is crucial for material and cell design. In this work the influence of grain size on the Li-ion conductivity of $\text{Li}_{7-3x}\text{La}_3\text{Zr}_2\text{Al}_x\text{O}_{12}$ ($x=0.22$) is presented. The synthesis and processing procedure allows changing the ceramic grain size, while maintaining the same synthesis parameters, eliminating influences of the synthesis on grain

boundary composition. Field assisted sintering technology is a powerful method to obtain dense, fine-grained ceramics with an optimal grain size of $2-3 \mu\text{m}$, where the conductivity is double that of the counterpart ($0.7 \mu\text{m}$). A total Li-ion conductivity of 0.43 mS cm^{-1} and an activation energy of 0.36 eV were achieved. The oxide-based all-solid-state battery cell combining the garnet-type electrolyte, a Li-metal anode and a thin-film LiCoO_2 cathode was assembled and cycled at room temperature for 90 hours. This represents a proof of concept, for the application of oxide-based electrolytes at ambient temperatures.

1. Introduction

Garnet-type ceramics (e.g., $\text{Li}_{7-3x}\text{La}_3\text{Zr}_2\text{Al}_x\text{O}_{12}$) are promising candidates as solid electrolytes for all-solid-state Li-ion batteries. Their chemical stability against Li-metal, which can potentially be used as an anode material, the charge carrier selectivity for Li-ions, thermal stability and, most importantly, the high room temperature bulk Li-ion conductivity of 0.59 mS cm^{-1} have motivated research on these materials.^[1,2] In addition to the phase purity of the material, it has been reported that the microstructure, i.e., pellet density and grain size, has a great influence on the electrochemical performance of the ceramic electrolyte.^[3,4] In the literature, there are attempts reported to determine the influence of the grain size on the Li-ion conductivity by utilizing different processing methods to achieve different grain sizes, e.g., FAST followed by conventional sintering for Ga-substituted $\text{Li}_3\text{La}_3\text{Zr}_2\text{O}_{12}$ or comparing ceramics synthesized using sol-gel methods with ceramics synthesized using solid state reactions.^[1,5] The first approach leads to substantial grain coarsening (from $1 \mu\text{m}$ to $7 \mu\text{m}$), in combination with a density increase. Because higher densities result in higher ionic conductivity, the two parameters cannot be separated from each other. Therefore, the influence of the grain size cannot be determined from such measurements. The second approach suggests a similar room temperature ionic conductivity for ceramics with a grain size of $3.3 \mu\text{m}$ compared to those with a grain size of 260 nm , with an activation energy of 0.26 eV and 0.41 eV , respectively.^[5] The use of different powder synthesis routes as an approach to vary the grain size also affects the phase composition and the microstructure. Furthermore, work by Cheng et al. suggests that reducing the grain size from $100-200 \mu\text{m}$ down to $10 \mu\text{m}$ leads to a slightly higher conductivity from 0.20 mS cm^{-1} to 0.25 mS cm^{-1} accom-

[a] Dr. M. Botros, Dr. T. Scherer, Dr. A. Kilmametov, Prof. H. Hahn
Institute of Nanotechnology, Karlsruhe Institute of Technology, Hermann-von-Helmholtz-Platz 1, 76344, Eggenstein-Leopoldshafen, Germany
E-mail: miriam.botros@kit.edu

[b] Prof. J. Gonzalez-Julian
Forschungszentrum Jülich GmbH, Institute of Energy and Climate Research, Materials Synthesis and Processing (IEK-1), 52425 Jülich, Germany

[c] Prof. J. Gonzalez-Julian
Institute of Mineral Engineering, Chair of Ceramics, RWTH Aachen University, 52074 Aachen, Germany

[d] Dr. R. Popescu
Laboratory for Electron Microscopy, Karlsruhe Institute of Technology, Engesserstr 7, 76131, Karlsruhe, Germany

[e] Dr. C. Loho
SCHOTT AG, Hattenbergstraße 10, 55122 Mainz, Germany

[f] Prof. O. Clemens
Institute for Materials Science, Materials Synthesis Group, University of Stuttgart, Heisenbergstraße 3, 70569 Stuttgart, Germany

[g] Dr. C. Loho, Prof. H. Hahn
Joint Research Laboratory Nanomaterials, Technische Universität Darmstadt, Alarich-Weiss-Str. 2, 64287, Darmstadt, Germany

[h] Dr. T. Scherer
Karlsruhe Nano Micro Facility (KNMF), Karlsruhe Institute of Technology, Hermann-von-Helmholtz-Platz 1, 76344, Eggenstein-Leopoldshafen, Germany

[i] Prof. H. Hahn
School of Chemical, Biological and Materials Engineering, The University of Oklahoma, 201 Stephenson Pkwy. Norman, OK 73019, USA

© 2024 The Authors. Batteries & Supercaps published by Wiley-VCH GmbH. This is an open access article under the terms of the Creative Commons Attribution Non-Commercial NoDerivs License, which permits use and distribution in any medium, provided the original work is properly cited, the use is non-commercial and no modifications or adaptations are made.

panied by a slight increase in activation energy from 0.32 eV to 0.34 eV. Additionally, an improvement of the area specific resistance against Li metal from $130 \Omega \text{cm}^2$ to $37 \Omega \text{cm}^2$ is observed.^[1]

In this work, the main objective is to study the influence of the grain size on the electrochemical performance, with minimal synthesis- and processing-related influences. Therefore, optional ball milling of the calcined powder, prepared by nebulized spray pyrolysis, is utilized followed by field assisted sintering to determine the influence of the initial particle size on the electrochemical performance of the dense $\text{Li}_{7-3x}\text{La}_3\text{Zr}_2\text{Al}_x\text{O}_{12}$ ceramic. The microstructural and compositional variations due to the additional ball milling step are discussed. During field assisted sintering the specimen is exposed to simultaneous heating at high heating and cooling rates, mechanical pressure and an electric field. The three components result in a fast sintering process at relatively low temperatures compared to conventional sintering methods, while maintaining a small grain size. The final grain size of the ceramic can thereby be varied by variation of the initial particle size of the powder in a controlled way. Additionally, the microstrain in the material is influenced by the field assisted sintering process.^[6] In this study the influence of the grain size and the correlated grain boundary contribution to the total conductivity is demonstrated. Additionally, the interfacial resistance at the electrolyte/Li-metal interface is characterized before and after cycling a symmetrical cell. Furthermore, a full all-solid-state battery cell with a Li-metal anode is assembled and characterized at room-temperature.

Experimental

Synthesis and Processing

The $\text{Li}_{7-3x}\text{La}_3\text{Zr}_2\text{Al}_x\text{O}_{12}$ ceramic powders were synthesized using nebulized spray pyrolysis (NSP) followed by a calcination step to achieve the desired garnet structure. The powder was then consolidated and sintered using field assisted sintering technology (FAST). During the NSP process the Al-doping can be precisely controlled to 0.22 mol Al. A detailed description of the NSP process can be found in previous work.^[7] The water-based precursor solution used for NSP (total cation concentration 0.05 mol l^{-1}) was prepared by first dissolving $\text{Zr}(\text{C}_5\text{H}_7\text{O}_2)_4$ (ABCR, 98%) in a small volume of methanol. The nitrate based precursors LiNO_3 (Sigma Aldrich, 99.99%), $\text{La}(\text{NO}_3)_3 \cdot 6\text{H}_2\text{O}$ (Alfa Aesar, 99.9%), and $\text{Al}(\text{NO}_3)_3 \cdot 9\text{H}_2\text{O}$ (Merck, 98.5%) were added to the methanolic solution and deionized water was added to the precursor solution to maintain the desired concentration. A water to methanol volume ratio of 30:1 was used. The as prepared mixture was then stirred for 1 h to produce a homogeneous transparent solution. A Li-excess of 30 wt.% was used to compensate for the Li-loss during heat treatment. The Li-loss is known to occur due to reaction of lithium oxide with water and carbon dioxide from the air to form Li_2CO_3 and its decomposition according to the sample environment.^[8] During annealing the powder was placed in a zirconia crucible and heated up to 900°C for 1 h under flowing argon atmosphere (0.2 slm) at ambient pressure. Argon was used to minimize the Li-loss.

The ceramics compared in this study are from the same batch of the NSP process. After calcination a defined amount of powder (approx. 300 mg) is used for FAST, while the remaining powder (approx. 1 g) is ball milled using Retsch PM100CM planetary ball mill. A 50 ml zirconia jar is used filled with 10 zirconia balls (diameter 10 mm). The speed is set to 500 rpm for 2 hours, with direction inversion every 30 min. The powder is filled and removed from the jar in an Ar-filled glove box. Field assisted sintering is carried out directly after ball milling, while the surfaces of the particles are activated and therefore show a higher reactivity and sinterability.^[9] The powders were placed in a graphite die surrounded by graphite foil. The foil was completely covered with boron nitride spray to prevent carbon diffusion into the sample. A temperature of 950°C was used with a holding time of 3 min. The heating rate was $100^\circ\text{C min}^{-1}$. The initial pressure applied during heating was approx. 5 MPa, while it was increased to 30 MPa and held for 3 min after reaching the sintering temperature. The pellet was then polished using grinding paper with grit sizes from 800 to 1200 grit.

In order to obtain an all-solid-state battery cell, thin-film cathode active material deposition on the electrolyte pellet represents a practical approach to ensure good contact at the interface and eliminates electronically conductive component, e.g., carbon black, and binders which hinder high temperature processing. The high temperature LCO phase is deposited on the polished pellet by means of a flash evaporation method, which relies on the non-equilibrium flash evaporation of a mixture of solid metal organic precursors of low volatility using a CO_2 laser.^[10] The powder precursors, cobalt(III)acetylacetone (Sigma Aldrich, 98%), and 2,2,6,6-tetramethyl-3,5-heptanedionato lithium (Sigma Aldrich, 98%), in molar ratio 1 to 3, are premixed under an inert gas atmosphere, and then transferred into a gas evaporation chamber for the evaporation with the CO_2 laser. In this process, the precursor vapor mixture is carried to the substrate using an argon gas flow, with an additional oxygen gas flow being introduced shortly before the vapor reaches the heated substrate. More detailed information about the synthesis procedure and setup are reported in previous work.^[11] In order to prevent changes to the microstructure and composition the $\text{Li}_{7-3x}\text{La}_3\text{Zr}_2\text{Al}_x\text{O}_{12}$ substrate during deposition, the substrate temperature is set to 700°C using an infrared laser temperature controlled by a pyrometer. The chosen temperature is a compromise between the goal of achieving a good contact between the solid electrolyte and thin-film cathode, while preventing Li loss from the substrate material. Furthermore, any chemical reaction between the two materials or elemental interdiffusion, which might occur at higher temperatures, are limited. The polished pellets as well as the half-cell are placed in an Ar-filled glovebox for contacting with the Li electrodes as previously reported.^[12]

Characterization Techniques

X-ray diffraction is used to determine the phase composition, lattice parameters as well as the microstrain, ϵ , of the analyzed samples (powders and pellets). The diffractograms are recorded using a Bruker D8 diffractometer with Bragg-Brentano geometry equipped with an X-ray tube with Cu anode, and a Ni filter for the removal of the K_β radiation. A VANTEC detector and a fixed divergence slit (0.3°) are used. The measurements are performed with a step size of 0.015° with a collection time of 1 s at 30 kV and 40 mA over the 2 θ angular range between 10° and 120° . The phase quantifications are performed by Rietveld analysis using the program TOPAS 4.2 (Bruker AXS, Karlsruhe, Germany). The quality of the Rietveld fit is measured by the weighted profile R-factor (R_{wp}), while the best possible R_{wp} is determined as the expected R-factor (R_{exp}). The

squared goodness of fit χ^2 is thereby defined as $(R_{wp}/R_{exp})^2$ and in an ideal scenario it is unity, but mostly it is larger.^[13,14] The instrumental intensity distribution for the X-ray data is determined empirically from a fundamental parameters set, using a reference scan of LaB₆ (NIST 660a).

The concentrations of the main elements Li, La, Zr and Al were determined by inductively coupled plasma optical emission spectrometry (ICP-OES, OPTIMA 4300 DV, PerkinElmer). The samples (2–3 mg) are dissolved in a mixture of 5 ml nitric acid and 5 ml sulfuric acid at 235°C for 3 h with the pressure digestion system DAB 2 (Berghof). Every sample has been digested three times. The acid solution was filled up to 50 ml and diluted in a ratio of 1:50 for the analysis of Li, La and Zr and 1:2.5 for the analysis of Al. The analyses were accomplished with four different calibration solutions and two internal standards (Na and Sc).

High-angle annular dark-field (HAADF) scanning transmission electron microscopy (STEM) combined with energy dispersive X-ray spectroscopy (EDXS) was used to investigate the microstructure and the chemical composition of the sample. The experiments are performed on an FEI Osiris ChemiSTEM microscope at 200 keV electron energy, equipped with a Super-X EDXS system comprising four silicon drift detectors. EDXS elemental maps of La (La-L_a line), Zr (Zr-K_a line), Al (Al-K_a line), O (O-K_a line) and C (C-K_a line) (contamination) are recorded and used to investigate their distribution within grains. We note here that Li cannot be detected by EDXS. Further, EDXS elemental maps are quantified to determine the average chemical composition of different regions on the sample. The quantification of EDXS maps was performed by using the ESPRIT software (version 2.3) from Bruker. Using ESPRIT, element concentrations are calculated on the basis of a refined Kramers' law model, which includes corrections for detector absorption and background subtraction. For this purpose, standardless quantification, i.e., by means of theoretical sensitivity factors, without thickness correction was applied. For HAADF STEM/EDXS experiments thin lamellae (50 nm) of the large and small grained ceramics are prepared using a Ga focused ion beam (FIB). A microstructural instability is observed during the FIB preparation especially around pores. This observation is most probably due to the decomposition of residual Li containing species like, e.g., Li₂CO₃ that are known for their beam sensitivity.^[15] This phenomenon increases with reduced thickness of the specimen, since it becomes more vulnerable to the electron beam as well as the ion beam during final polishing of the lamellae. Nevertheless, the grains and the grain boundaries without any large pores, where the beam sensitive species presumably reside, remain stable during FIB preparation. The lamellae are transferred to the transmission electron microscope for further characterization after only a few minutes of air exposure.

The microstructure of the powders and sintered ceramics were studied using a scanning electron microscope, SEM (Philips XL30 FEG) operating at 10 kV. Prior to imaging the ceramic samples were broken manually. The cross section was sputtered with Au for electrical conductance in addition to the carbon tape and silver paste used to attach the sample to the sample holder. The particle size of the powders and the grain size of the sintered ceramics were determined from the mean value of over 100 measurements (ImageJ). Electrochemical characterization was performed using Electrochemical Impedance Spectroscopy (EIS). After gold coating (Quorum Q300TD, approx. 100 nm) the pellets are placed in a cryostat (Janis STVP-200-XG) with brass connection plates directly contacted to the gold electrodes. The cryostat allowed for measurements in the temperature range between 200 K and 393 K. The frequency range used for all measurements was 1 MHz down to 0.1 Hz with a collection rate of 50 points per decade and a potential amplitude of 20 mV. Cyclic voltammetry and galvanostatic cycling

(Solartron Analytical 1470E/1455) are performed on cells mounted inside Swagelok type connections containing a spring for the application of a constant pressure to ensure good electrical and thermal contact during cycling. A temperature cabinet (Memmert IPP 260) is used to ensure stable temperatures.

The full all-solid-state cells with the LiCoO₂ thin-film cathode, the solid electrolyte and the lithium anode is placed in a Swagelok-type cell, with the cells being fixed using a spring without additional pressure. After a resting step for 24 hours to reach electrochemical and thermal equilibrium, 5 cycles of galvanostatic cycling are performed at 500 nA between 3 V and 4.2 V vs. Li/Li⁺. Then, cyclic voltammetry is performed at 0.1 mVs⁻¹ for 5 cycles before the current is again set to 500 nA for further 10 cycles and reduced to 250 nA for 10 additional cycles. A calculation of the C-rate would be highly inaccurate, since the volume of the cathode layer can only be roughly estimated. All cycling experiments are performed at 25°C using a temperature cabinet to maintain a constant temperature.

2. Results and Discussion

2.1. Structure and Chemical Composition

The phase composition of the calcined powder as well as after ball milling is shown in Figure 1a. Rietveld refinement of the calcined powder shows a mixture of cubic and tetragonal phase with 47.5 wt.% and 51.4 wt.%, respectively. Additionally, 1 wt.% of Li₂ZrO₃ is detected. The crystallite size lies in the range of a few hundred nanometers and cannot be accurately determined and therefore is fixed to approximately 300 nm during Rietveld refinement. After ball milling a broadening of the reflections is observed indicating a decrease in crystallite size down to approximately 15 nm. The presence of impurity phases is negligible for both starting materials. After field assisted sintering the pellets are measured on both sides and the corresponding X-ray diffractograms are shown in Figure 1b. Comparable results are observed concerning the emerging of a tetragonal phase resulting from straining (more details are reported in^[16]) as well as the presence of a La₂Zr₂O₇ impurity phase, which is indicative for Li loss from the garnet structure during sintering. An overview of the Rietveld refinement data for the sintered ceramics are presented in Table 1. The values given are mean values of measurements taken on both sides of the pellets. The variation of the fraction of the impurity phase on both sides of the ceramic sample most probably originates from the electromigration of the Li-ions due to the direct current electric field applied during field assisted sintering. The most prominent difference between the sintered ceramics besides the grain size is the amount of La₂Zr₂O₇ impurity phase. The mean value of the impurity phase fraction for the ceramic sintered after ball milling of the starting powder is significantly higher than for the ceramic sintered directly after calcination. This fact has to be taken into consideration, since the electrochemical performance might suffer due to the presence of the La₂Zr₂O₇ phase.

The higher amount of the La₂Zr₂O₇ impurity phase is an indication of Li loss from the garnet structure and thereby possibly reducing the charge carrier concentration, i.e., Li-ion

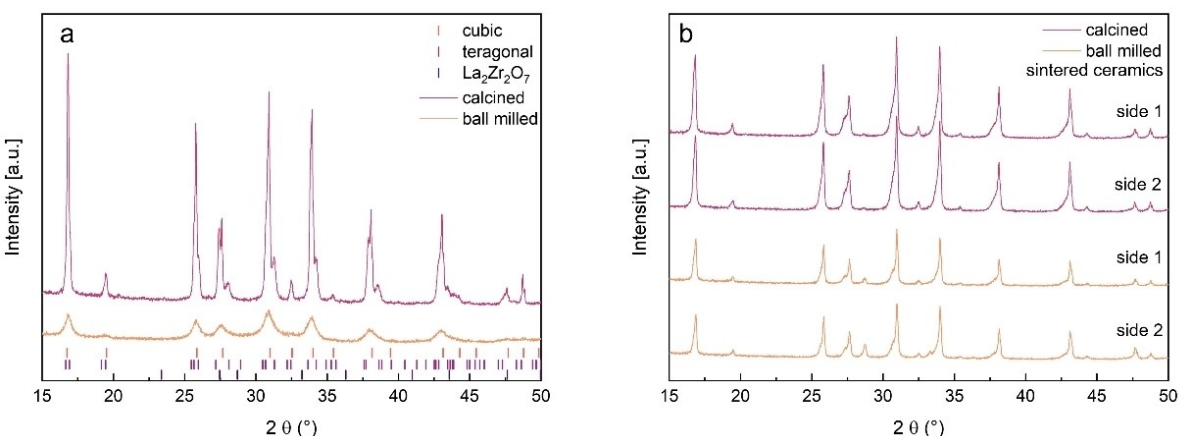


Figure 1. X-ray diffraction patterns of the $\text{Li}_{7-x}\text{La}_3\text{Zr}_2\text{Al}_x\text{O}_{12}$ calcined powder with $x = 0.22$ at 900°C for 1 h and followed by ball milling at 500 rpm for 2 h (a) and respective sintered ceramics measured on both sides of the pellets (side 1 and side 2) (b).

Table 1. Rietveld refinement data for sintered ceramics with calcined and additionally ball milled starting material with $x = 0.22$.

Sample	Phase	Phase fraction [wt.%]	Unit cell volume [\AA^3]	Microstrain [%]	c/a
Sintered ceramic (calcined)	cubic	50.7(2)	2175.669(94)	0.036(4)	1
	dis. tetragonal	49.0(2)	2211.0(16)	0.333(2)	0.992
	La ₂ Zr ₂ O ₇	0.31(2)	1260.4(14)	-	1
Sintered ceramic (calcined + ball milled)	cubic	57.6(1)	2176.73(14)	0.047(4)	1
	dis. tetragonal	38.8(1)	2216.2(13)	0.346(3)	0.992
	La ₂ Zr ₂ O ₇	4.6(2)	1262.43(29)	-	1

concentration for ionic conductivity. To confirm the Li loss, ICP-OES measurements are carried out for ceramics sintered with a starting material directly after calcination and after an additional ball milling step. The results are shown in Table 2. It is evident that the Li amount in the sample showing a higher impurity phase fraction is indeed 9% lower, but the Li-content for both samples is higher than the nominal value for the garnet phase. This might be due to the Li-excess used during synthesis, which may partially still be present occupying Li-sites in the garnet structure or as a Li-containing compound (e.g., Li₂O, Li₂CO₃) not detected by X-ray diffraction. The amount of Li-ions involved in the conduction process, that reside on tetrahedral and octahedral sites, is estimated to be only 12.3% of the total Li-ion concentration in the garnet structure.^[17] Therefore, a possible Li loss from the garnet structure due to the processing route including ball milling does not necessarily mean a loss of charge carriers for the conduction process. A high Li occupancy, however, could reduce the Li-ion mobility due to the reduced number of Li vacancies and explains the presence of the tetragonal phase after calcination. Additionally,

the fast cooling rate typical for field assisted sintering can increase Li ordering in the structure, reducing ion mobility.^[18]

For the characterization of the microstructure of the calcined powder before and after ball milling as well as the corresponding sintered ceramics, scanning electron microscopy is utilized. The micrographs for the powders and cross sections of the sintered ceramics are presented in Figure 2. The calcined powder shows large agglomerates consisting of solid particles. Sintering necks are formed between the particles indicating the onset of the sintering process. After ball milling the sintering necks are no longer observed and the particle size ranges from 0.2 μm to 3.3 μm , with a mean value of 0.9 μm . Nevertheless, agglomeration is still present. After field assisted sintering of the calcined powder the pellet is broken manually to investigate the cross section. The micrograph shows a high density, as expected from density measurements using a novel method employing laser confocal microscopy. A detailed description of the method is reported elsewhere.^[19] The measured density is 5.11(5) g cm^{-3} (> 99% TD). Grain sizes between 1.1 μm and 5.9 μm have been measured on 100 grains with a mean value

Table 2. ICP-OES results for sintered ceramics, nominal composition $\text{Li}_{6.34}\text{La}_3\text{Zr}_2\text{Al}_{0.22}\text{O}_{12}$, with different grain sizes due to additional ball milling of the starting powder after calcination.

Sample	Li [mol]	Al [mol]	Li:La	Li:Zr	Zr:La
Calcined	7.14(24)	0.196(2)	2.38	3.35	0.68
Calcined + Ball milled	6.50(06)	0.217(2)	2.17	3.16	0.68

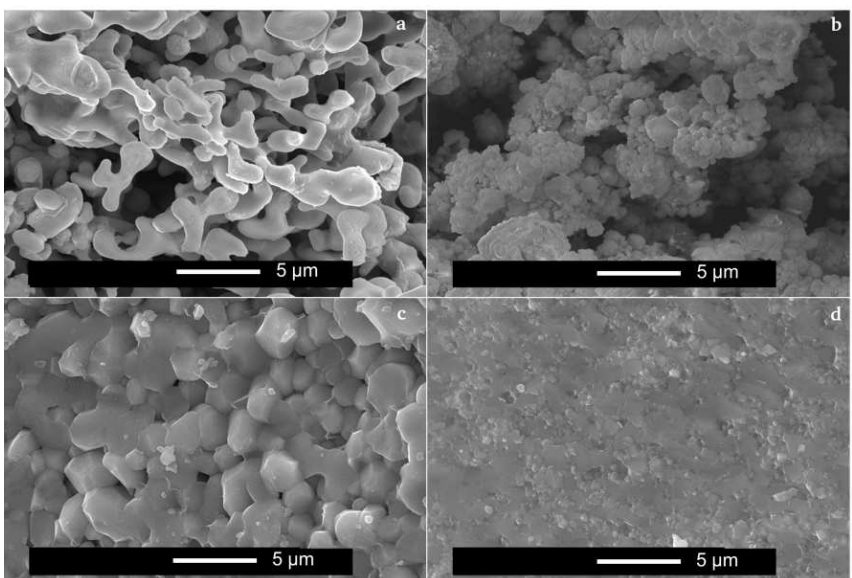


Figure 2. SEM images of calcined $\text{Li}_{7-x}\text{La}_3\text{Zr}_2\text{Al}_x\text{O}_{12}$ powder ($x=0.22$) before (a), after (b) ball milling and the corresponding large (c) and small grained ceramics (d).

of $2.2 \mu\text{m}$. The cross-sectional imaging of the ceramic sintered using the ball milled powder shows a significantly smaller grain size between $0.2 \mu\text{m}$ and $1.7 \mu\text{m}$ with a mean value of $0.7 \mu\text{m}$ and a high density of $4.97(5) \text{ g cm}^{-3}$ (97% TD).

A more detailed characterization of the microstructure, especial of the inter- and intragranular elemental distribution and their chemical composition, is carried out using HAADF STEM combined with EDXS. The EDXS elemental maps of Zr (K_α -line), La (L_α -line), Al (K_α -line), O (K_α -line) and C (K_α -line) for the large-grained ceramic are shown in Figure 3. We note that the EDXS elemental map of the Al distribution within the sample shows no segregation of Al at the grain boundaries, but being uniformly distributed within the $\text{Li}_{7-x}\text{La}_3\text{Zr}_2\text{Al}_x\text{O}_{12}$ grains (Figure 3d). Furthermore, EDXS elemental maps indicate the uniform distribution of Zr and La within grains (Figure 3 b–c), while the quantitative analysis of the EDXS C map results in a low C contamination level within grains of approximately 2 at.% (Figure 3 f). However, the HAADF STEM image shows the formation of circular pores within some grains. EDXS investigations indicate no segregation of Al, as well as, of any other

element in regions where the observed pores reside. It can be ruled out that pores are an artefact due to sample preparation, since the second sample with a smaller grain size, prepared under the same conditions, does not exhibit intragranular pores. The agglomerated calcined powder with sintering necks between the particles might be the origin for the pore formation. The chemical composition of some regions on the large-grained ceramic is determined by the quantification of EDXS elemental maps recorded within dashed frames shown in Figure 3 g–h and the corresponding results are given in Table 3. The quantitative analysis shows the formation of grains with the stoichiometric $\text{Li}_{6.1}\text{La}_{3.0}\text{Zr}_{2.0}\text{Al}_{0.3}\text{O}_{12.0}$ composition (Table 3). Here, the Li-content n_{Li} , which cannot be determined by EDXS, was calculated from the measured Al-content x_{Al} for the intragranular regions with and without pores by using the relation:

$$n_{\text{Li}} = 7 - 3x_{\text{Al}} \quad (1)$$

Table 3. EDXS quantitative results of the selected regions of the large grained ceramic.

Region	La [mol]	Zr [mol]	Al [mol]	O [mol]	C [mol]
1	3.20(30)	2.00(20)	0.28(04)	11.5(6)	–
2	3.20(30)	2.00(20)	0.26(04)	12.0(6)	–
3	3.20(30)	2.00(20)	0.28(04)	12.3(6)	–
4	3.30(30)	2.00(20)	0.28(04)	13.3(9)	–
5	3.20(32)	2.00(20)	0.28(04)	9.1(8)	–
6	3.10(25)	2.00(20)	0.22(04)	10.6(9)	–
7	3.10(26)	2.00(20)	0.18(03)	7.6(3)	0.24(03)
8	3.22(42)	2.00(35)	0.23(06)	21.6(9)	5.16(22)

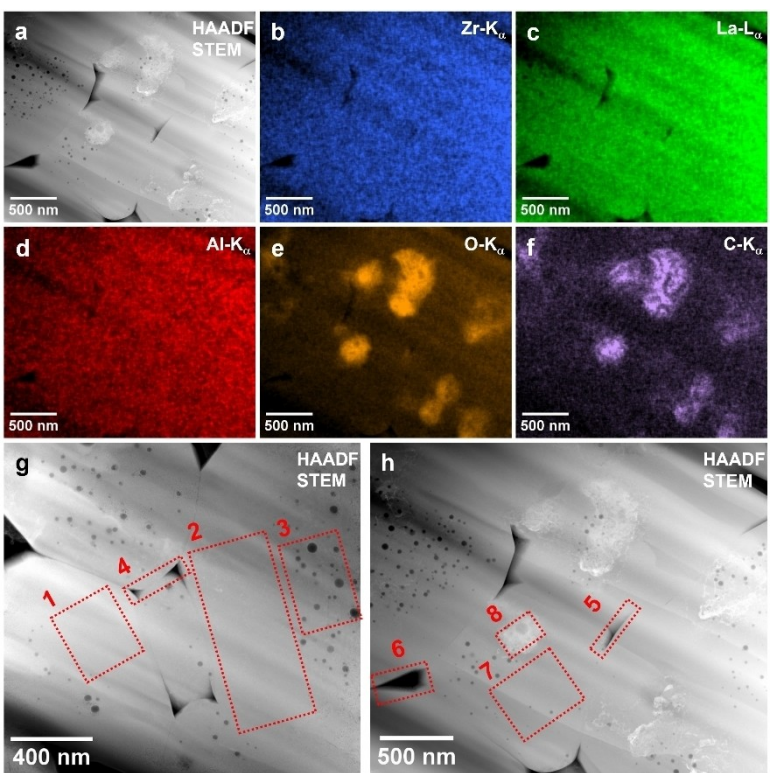


Figure 3. (a) HAADF STEM image and corresponding EDXS elemental map distributions of (b) Zr (K_{α} -line, blue), (c) La (L_{α} -line, green), (d) Al (K_{α} -line, red), (e) O (K_{α} -line, orange) and (f) C (K_{α} -line, lavender) of sintered $\text{Li}_{7.3x}\text{La}_3\text{Zr}_2\text{Al}_x\text{O}_{12}$ ($x=0.22$) large grained ceramic; (g)–(h) HAADF STEM images with frames showing the regions used for EDXS map quantification: (g) grains without precipitates and (h) grains with Li_2CO_3 precipitates.

In addition, the grain boundary regions exhibit about the same chemical composition as the inner parts of the grains of $\text{Li}_{6.1}\text{La}_{3.0}\text{Zr}_{2.0}\text{Al}_{0.3}\text{O}_{12.0}$, confirming the formation of a stoichiometric compound. However, the HAADF STEM image in Figure 3a shows the precipitation of a secondary phase with a brighter contrast compared to that of the grains. Due to the Z-contrast of HAADF STEM images, which is related to the average atomic number of chemical elements of the material, different chemical composition of precipitates and grains is expected. This is supported also by EDXS elemental maps of O and C distributions, which show that the precipitated material contains more O and C compared to grains (Figure 3 e–f).

A significant sub-stoichiometric oxygen composition of grains containing precipitated material in comparison to that of grains without any precipitated phase is noted. By investigating the precipitated phase composition, it has to be accounted for that the chemical composition determined by the quantification of EDXS spectra recorded from grains with precipitates (like that within frame 8 in Figure 3h) is a weighted sum of the precipitate composition and the composition of the grain under the precipitate. Accordingly, to determine the real composition of the precipitated phase, the chemical composition of the same grain in a region without precipitate has to be separately measured and subtracted from the chemical composition determined for the grain region containing the precipitate. After subtracting the composition of the grain from the composition of the grain and the precipitated phase, the ratio

of C to O was calculated to 1:2.9 for the precipitate material located within frame 8 in Figure 3h. Firstly, we note that, within the experimental error, the precipitated phase does not contain any La, Zr or Al. Hence, the measured composition of $\text{C}_1\text{O}_{2.9}$ corresponds to the real composition of Li_2CO_3 for the precipitated phase by taking into account that Li cannot be determined by EDXS. This chemical composition is further confirmed by the quantification of the EDXS map recorded from another place containing the segregated material, which is located in a different grain. The oxygen deficiency of the garnet phase around the segregated material as well as the confirmation that the segregation is a carbonate containing phase, leads to the conclusion that oxygen as well as Li are extracted from the garnet structure during sintering and react with carbon contamination most probably from adsorbed CO_2 during the short transport of the powder in air. Summarizing, all chemical compositions determined by EDXS are similar to each other within the experimental error and indicate a sub-stoichiometric oxygen composition for grains containing the precipitated Li_2CO_3 phase.

EDXS maps are further used to determine the chemical composition of regions at the grain boundaries (dashed frames 4, 5 and 6 in Figure 3 g–h, quantification results in Table 3). No compositional change is expected from the visual inspection of EDXS elemental maps. Firstly, an Al-content between $x=0.20$ and $x=0.30$ throughout all measurements and no Al segregation is noted. Then, as expected, the grain boundary regions,

which do not contain precipitated phase (dashed frame 4 in Figure 3 g) have the same composition of $\text{Li}_{6.1}\text{La}_{3.0}\text{Zr}_{2.0}\text{Al}_{0.3}\text{O}_{12.0}$ like the corresponding inner grains. However, the sub-stoichiometric oxygen content of grain boundaries between grains containing the precipitated phase (dashed frame 5 and 6 in Figure 3h) might indicate the formation of the Li_2CO_3 phase also in the corresponding grain boundary region during sintering. This phase is not visible on the HAADF STEM image due to its decomposition during field assisted sintering or FIB processing. The formation of a neutral Schottky-like defect pair $2V_L^x + V_O^x$ is energetically favorable according to a theoretical study,^[20] which might explain the oxygen deficiency due to Li_2CO_3 formation.

The EDXS elemental maps of Zr (K_{α} -line), La (L_{α} -line), Al (K_{α} -line), O (K_{α} -line) and C (K_{α} -line) for the small-grained ceramic are shown in Figure 4. The C contamination level is low, the quantification of the EDXS data results in a level <2 at.%, similar to that of large grains discussed above. Similar to the large-grained ceramic, the EDXS elemental map of Al distribution shows no segregation of Al at the grain boundaries, but rather a uniform distribution across the small $\text{Li}_{7-3x}\text{La}_3\text{Zr}_2\text{Al}_x\text{O}_{12}$ grains (Figure 4 d). An exception is represented by the grain with the high contrast on the HAADF STEM image in Figure 4 a. The Z-contrast of HAADF STEM images indicates a different chemical composition of this particular grain compared to that of the neighboring grains. This assumption is further supported from the EDXS elemental maps of the Zr and Al distributions

(Figure 4 b–c), which show that this grain contains more Zr (with a high atomic number Z) and less Al (with a small atomic number Z) compared to the other grains. The rectangles indicated by dashed lines in the HAADF STEM images shown in Figure 4 g–h) represent the regions where the chemical composition within the small grain sample were investigated. The corresponding compositions are given in Table 4. The quantification of EDXS maps recorded from regions entirely located within grains with the exception of the grain with a higher contrast, demonstrates their stoichiometric $\text{Li}_{6.1}\text{La}_3\text{Zr}_2\text{Al}_{0.3}\text{O}_{12}$ composition (Figure 4 g–h). We note again that Li cannot be detected by EDXS and then, the Li-content x_{Li} is calculated on the basis of the Al-content x_{Al} according to Eq. (1). On the other hand, grains with a brighter contrast in Figures 4 a, g and h show a chemical composition, which corresponds to that of the $\text{La}_2\text{Zr}_2\text{O}_7$ phase with a similar La content as the other grains (18 at.%) but more Zr (18 at.%) compared to 11 at.%) and almost no Al. The quantification of grain boundary regions results, as expected from the visual inspection of EDXS elemental maps in Figure 4 b–f, in chemical compositions, which are in agreement with the stoichiometric composition of $\text{Li}_{6.1}\text{La}_3\text{Zr}_2\text{Al}_{0.3}\text{O}_{12}$ grains. Therefore, it is concluded that the impurity $\text{La}_2\text{Zr}_2\text{O}_7$ phase that forms due to Li-loss from the garnet structure^[8] is localized as separate grains and is not distributed along grain boundaries. This suggests a low impact of these impurities on the Li-ion conductivity, since

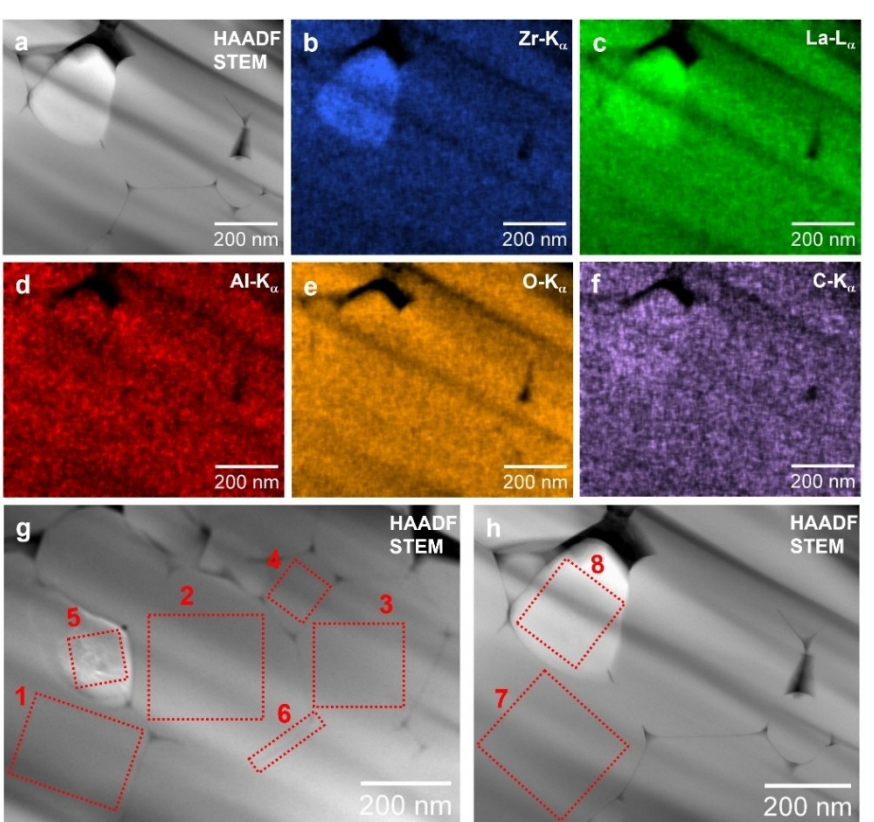


Figure 4. (a) HAADF STEM image and corresponding EDXS elemental map distributions of (b) Zr (K_{α} -line, blue), (c) La (L_{α} -line, green), (d) Al (K_{α} -line, red), (e) O (K_{α} -line, orange) and (f) C (K_{α} -line, lavender) of sintered $\text{Li}_{7-3x}\text{La}_3\text{Zr}_2\text{Al}_x\text{O}_{12}$ ($x=0.22$) small grained ceramic; (g)–(h) HAADF STEM images with frames used for the EDXS map quantification.

Table 4. EDXS quantitative results for the selected regions of the small grained ceramic.

Region	La [mol]	Zr [mol]	Al [mol]	O [mol]
1	3.20(30)	2.00(20)	0.34(04)	12.3(8)
2	3.20(30)	2.00(20)	0.32(04)	12.4(6)
3	3.20(30)	2.00(20)	0.34(04)	11.6(6)
4	3.10(30)	2.00(20)	0.28(04)	12.3(9)
5	1.97(28)	2.00(22)	0.03(2)	6.7(2)
6	3.10(32)	2.00(20)	0.28(04)	12.5(8)
7	3.00(26)	2.00(20)	0.26(03)	11.3(9)
8	2.06(27)	2.00(22)	0.06(2)	6.1(3)

the charge carriers are expected to choose the pathway with the lowest resistance avoiding localized impurities.

Neither intragranular pores nor Li_2CO_3 grain inclusions are detected in the small-grained ceramic, which is caused by the favorable microstructure and results in favorable sintering properties of this particular starting material. As previously mentioned, Li_2CO_3 grain inclusions are most probably formed due to the CO_2 adsorption on the surface of the particles prior to sintering. This assumption is supported by the sub-stoichiometric oxygen content of the grains showing Li_2CO_3 inclusions, while pure LLZO grains in the large- and small-grained ceramics show a stoichiometric oxygen content. Therefore, it is assumed that during field assisted sintering the highly mobile Li reacts with the adsorbed CO_2 extracting oxygen (resp. Li_2O) from the garnet structure. The particle surfaces, where this reaction takes place can be both intra- and intergranular in the case of the large-grained ceramic. In the case of the small-grained ceramic, on the other hand, the particle surfaces, which are expected to

have a higher reactivity due to ball milling, thus form the grain boundaries of the sintered ceramic (see schematic in Figure 5). For both ceramics no intergranular Li_2CO_3 phase is detected, which might indicate its decomposition during the sintering process at 950°C forming gaseous CO_2 and solid Li_2O . This process is expected to have a significant influence on the ionic conductivity at the grain boundaries.

2.2. Electrochemical Characterization

To determine the influence of the grain size on the ionic conductivity AC-impedance spectroscopy is carried out with blocking Au-electrodes. The advantage of performing the measurements at low temperatures, as low as 220 K, is the possibility to separate the bulk and the grain boundary contributions for samples with different grain sizes. The Nyquist plots are shown in Figure 6 with arrows indicating the

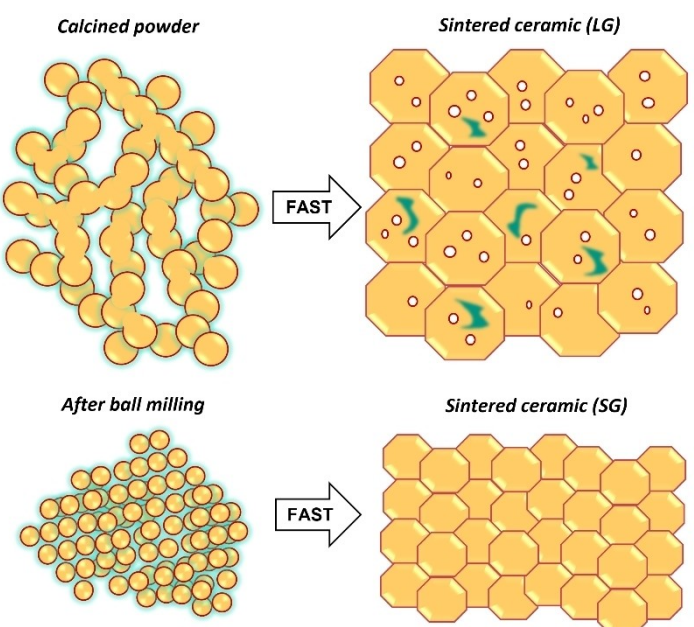


Figure 5. Schematic of the calcined powders before and after ball milling (left) and sintered large-grained (LG) and small-grained (SG) ceramics (right). LG ceramics show pores (white) and Li_2CO_3 inclusions (green) originating from surfaces of agglomerated particles (red). SG ceramics show dense grains with no Li_2CO_3 inclusions.

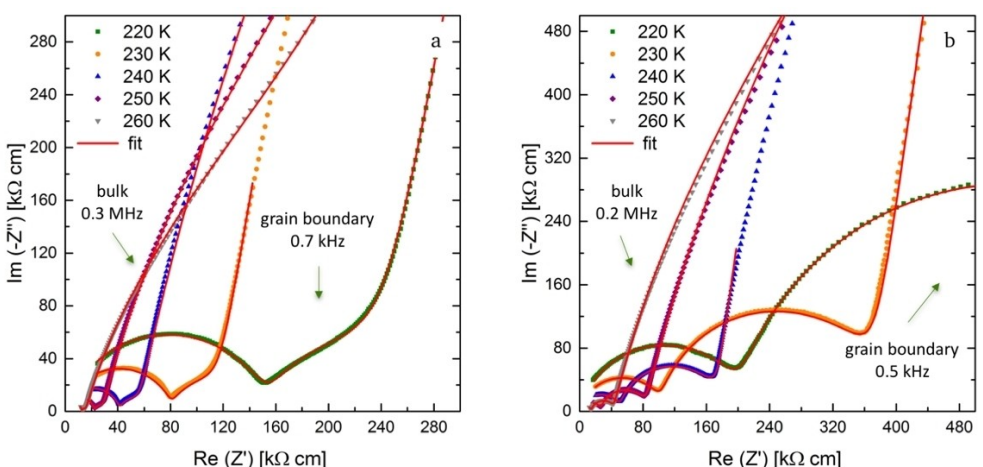


Figure 6. Nyquist plots and corresponding fits for sintered ceramics ($x = 0.22$) with blocking Au-electrodes at 220 K up to 260 K with calcined (a) and calcined then ball milled starting powder (b). Arrows indicate the frequency at the maxima of the respective semi-circle marked on the spectrum measured at 220 K (red dots).

frequencies at the maximum point of each semi-circle at the lowest temperature. Equivalent circuits are chosen to fit the detected semi-circles at each temperature. At low temperatures, $R(R \text{ CPE})(R \text{ CPE})\text{CPE}$ is employed since the surface layer contribution expected at low frequencies is not detected. Starting at 240 K, the equivalent circuit $R(R \text{ CPE})(R \text{ CPE})(R \text{ CPE})\text{CPE}$ is used to fit the spectra. The normalized resistance values show an increase in both bulk and grain boundary contributions to the spectrum for the ceramic with smaller grain size. The increase in bulk resistance is not expected to be affected by the grain size. Thus, the increase of approximately 23% could result from the increased Li loss from the garnet structure due to the smaller grain size and the formation of $\text{La}_2\text{Zr}_2\text{O}_7$ grains, as observed from HAADF STEM. Since the Li loss mechanism is governed by the presence of moisture and CO_2 a finer grain size and thus a larger surface area of the particles allows for the adsorption of a larger amount of these species leading to a higher reactivity with Li during the sintering process. The normalized resistance is approximately 67% higher for the ceramic with a smaller grain size compared to the large-grained ceramic. This increase in grain boundary resistance indicates that an additional transport phenomenon is induced, which is likely assigned to the increased number of grain boundaries due to the smaller grain size, leading to a higher grain boundary resistance. The room temperature total conductivities for large grained and small grained ceramics are $0.43 \text{ mS}\text{cm}^{-1}$ and $0.23 \text{ mS}\text{cm}^{-1}$, respectively.

The Arrhenius plot, i.e., the temperature dependence of the total conductivity, is shown for both samples in Figure 7a. The ceramic prepared from calcined powder shows higher conductivities throughout the whole temperature range and an activation energy of 0.36 eV. On the other hand, the ceramic with a smaller grain size due to the additional ball milling step of the starting material shows an activation energy of 0.40 eV. In addition to the decrease of the bulk and grain boundary conductivities the activation energy is significantly increased for the ceramic with a smaller grain size. This indicates that an

increase in the amount of grain boundaries decreases the Li-ion mobility, which is the determining factor for the electrochemical performance.^[21] The Li-ion conductivity is defined as follows:

$$\sigma_{Li} = qc\mu_{Li} \quad (2)$$

Where q is the charge, c the charge carrier concentration and μ_{Li} is the ion mobility. Assuming constant q and c , the increased volume fraction of grain boundaries reduces ion mobility and thereby the conductivity. Additionally, the temperature dependance of the conductivity is described as follows:

$$\sigma_{Li} = \frac{\sigma_0}{T} e^{-\frac{E_a}{k_B T}} \quad (3)$$

Where σ_0 accounts for the entropy of migration, the jump distance, the jump attempt frequency and geometric factor depending on the directionality of the conduction mechanism, T is the absolute temperature and E_a the activation energy meaning the energy barrier an ion has to overcome for a successful jump and k_B is the Boltzmann constant.^[22,23] Thereafter, the activation energy is one of the determining factors of Li-ion conductivity, while ideally σ_0 has to remain constant for a direct comparison of different samples.

For further evaluation of both bulk and grain boundary effects occurring as a result of the decreased grain size the respective conductivities are calculated using the dimensions of the pellet for both values. This is only an approximation, since the real thickness to surface ratio is expected to be larger for the grain boundary conductivity than for the bulk conductivity leading to higher values for the grain boundary conductivity than reported here. A direct comparison of the temperature dependence of the bulk and grain boundary conductivities is given in Figure 7 b and c. The sample with a large grain size shows higher grain boundary conductivities than the bulk conductivities throughout the entire temperature range, while

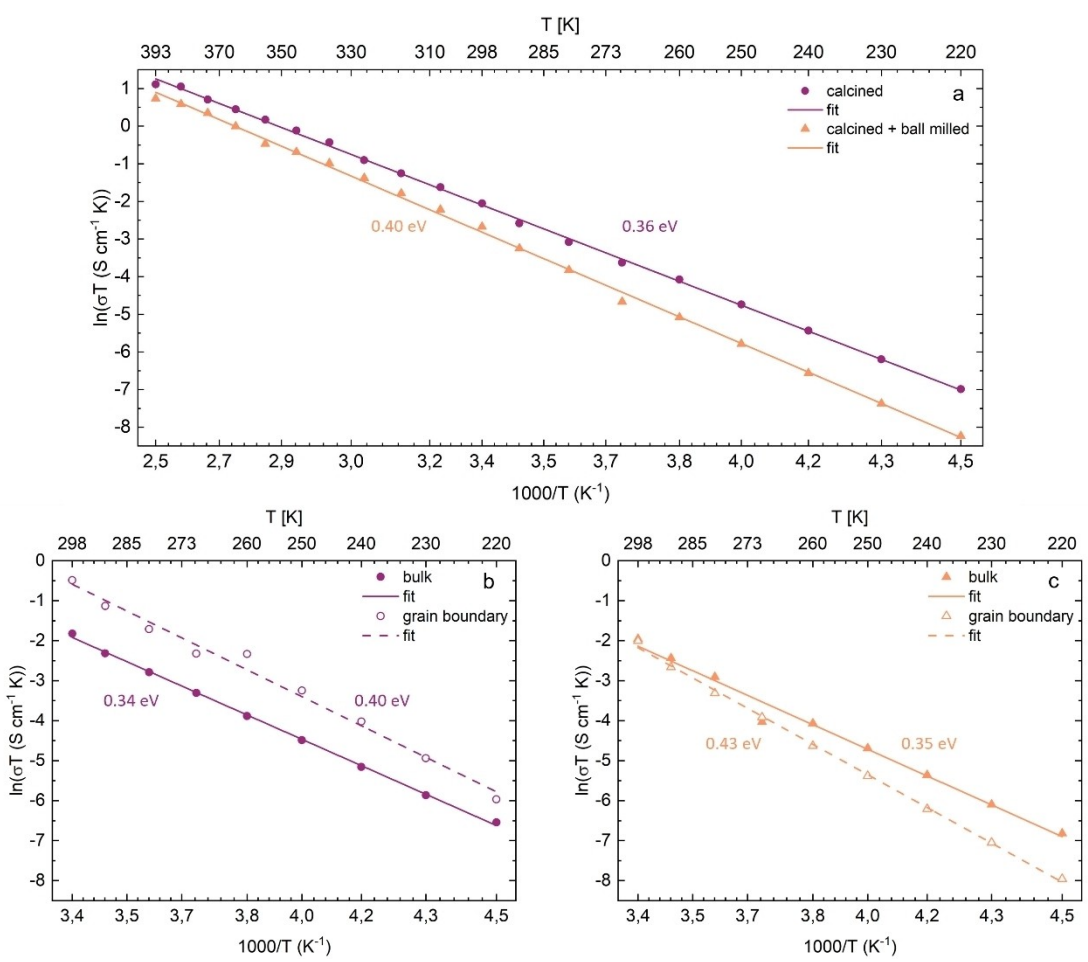


Figure 7. Arrhenius plots presenting the temperature dependence of the total Li-ion conductivity for two different grain sizes achieved by ball milling of the starting powder (a) and of the bulk and grain boundary Li-ion conductivities between 220 K and 298 K for two different grain sizes: large grained (b) and small grained ceramic (c).

the bulk and grain boundary activation energies are calculated to be 0.34 eV and 0.40 eV, respectively. The ceramic with a smaller grain size does not only show an increase in grain boundary resistance but also an increase in the grain boundary activation energy up to 0.43 eV, while the bulk activation energy only increased to 0.35 eV. The small bulk activation energies are in good agreement with ^{7}Li pulsed field gradient nuclear magnetic resonance (PFG-NMR) results reported in literature, which confirm fast local ion motion in the bulk and therefore deliver the lowest expected value of 0.32 eV.^[24] Again, this indicates that Li loss during sintering and the increased formation of the $\text{La}_2\text{Zr}_2\text{O}_7$ impurity phase has a much lower impact on the activation energy, which is observed for the bulk, while the impact of the larger amount of grain boundaries is more significant for the grain boundary conductivity as well as the activation energy. The increase in activation energy is also observed in literature for a similar grain size region for samples produced using two different synthesis methods. It has been reported that the ceramic with a smaller grain size shows a similar room temperature conductivity and higher conductivities for temperatures above 312 K.^[5] These findings lead to the conclusion that the ionic mobility is reduced in the ceramic

with a smaller grain size ($0.7 \mu\text{m}$) compared to the large grained ceramic ($2.2 \mu\text{m}$).

According to the literature a decrease of the grain size from a few hundred microns to $40 \mu\text{m}$ leads to an enhancement of the cycling stability against Li metal.^[1] In this study the grain size is reduced from $2.2 \mu\text{m}$ to $0.7 \mu\text{m}$, which covers a different range than previously reported. For the characterization of the electrochemical stability against Li metal the large- and small-grained ceramics are contacted on both sides with Li metal electrodes. Two different current densities are used, $50 \mu\text{A cm}^{-2}$ and $75 \mu\text{A cm}^{-2}$. Galvanostatic cycling results are depicted in Figure 8. The large grained ceramic shows a very good electrochemical stability at the initial current density ($50 \mu\text{A cm}^{-2}$) for 10 cycles, while the cell potential shows a slight increase of approximately 1 mV during each cycling step upon cycling at the higher current density for 5 cycles. The following 10 cycles at the initial current density show stable cycling with no significant change compared to the first 10 cycles. On the other hand, the small grained ceramic (half pellet was used) shows great instability in the first 5 cycles at $50 \mu\text{A cm}^{-2}$, which stabilizes starting from the sixth cycle but showing an increase in cell potential in each step of at least 7 mV. Increasing the

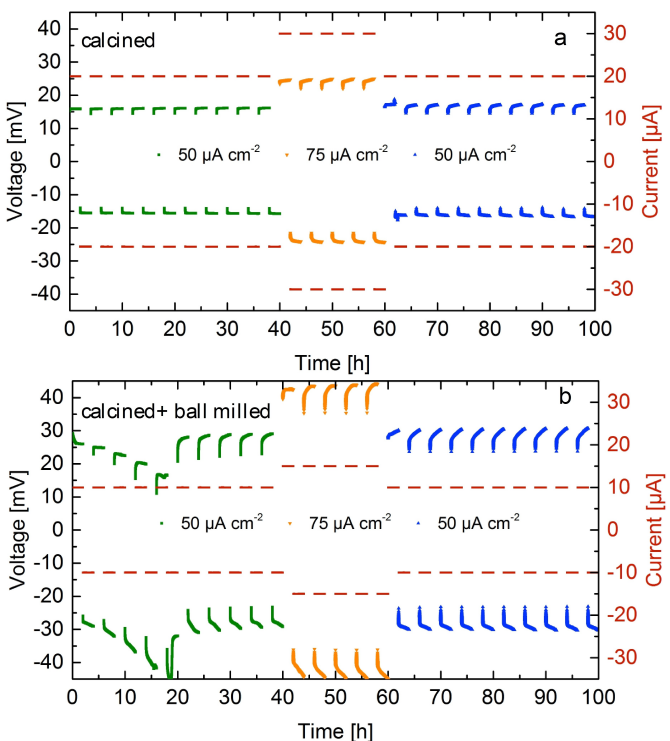


Figure 8. Galvanostatic cycling of symmetrical cells Li|LLZO|Li at different current densities for ceramics with $x = 0.22$ prepared from two different starting powders: calcined (a) and calcined then ball milled (b).

current density leads to the expected increase in cell potential and an additional increase during each step of at least 8 mV. The subsequent cycles at the initial current density show symmetrical cell potential during charge and discharge with an increase of 7 mV during each cycling step. It is indicated that the sample with larger grain size shows improved electrochemical stability against Li metal and that increasing the current density above $50 \mu\text{A cm}^{-2}$ leads to a slight degradation of the cell.

A more stable cycling performance of the small grained ceramics might be expected due to the larger area available for

Li formation at the interface between Li and the garnet material. For a large grained ceramic ($100\text{--}200 \mu\text{m}$), the current pathways are limited since the current accumulates in the regions with highest conductivity creating current spikes and could accelerate dendrite formation. On the other hand, when there is a larger number of high conductivity regions (grain boundaries) the current distribution is more homogeneous throughout the interface between Li and the solid electrolyte with a smaller grain size ($40 \mu\text{m}$).^[1] In the present study this argument holds true for grain sizes down to $2.2 \mu\text{m}$, where the current is homogeneously distributed and the cell is stable during cycling for 100 hours. Whereas, reducing the grain size further to $0.7 \mu\text{m}$ the grain boundary conductivity evidently decreases and is comparable to the bulk conductivity at room temperature. This might explain the observed instability of the interface during cycling in the first 5 cycles, where the current pathways are formed throughout the interface. There is no clear pathway with a higher ionic mobility, therefore, the Li-ion flow needs more time to stabilize and the cell exhibits higher cell potentials due to the higher resistances compared to the large grained ceramic ($2.2 \mu\text{m}$).

AC-impedance spectroscopy was carried out to obtain a deeper understanding of the findings of the galvanostatic cycling and to determine the area specific resistance (ASR) at the interface between the solid electrolyte and Li metal. The Nyquist plots for measurements with blocking Au-electrodes as well as non-blocking Li-electrodes at room temperature are shown in Figure 9. The measurements with non-blocking Li-electrodes were conducted before cycling, after 10 cycles at $50 \mu\text{A cm}^{-2}$, after additional 5 cycles at $75 \mu\text{A cm}^{-2}$ and after 10 additional cycles at the initial current density. The total resistance of the symmetrical cell before cycling is $0.79 \text{ k}\Omega$ for the ceramic with a larger grain size, while it is $2.73 \text{ k}\Omega$ for the small grained ceramic. These values are in good agreement with the total cell resistance calculated from galvanostatic cycling. The fits of the spectra are carried out using R(R CPE)(R CPE) equivalent circuit, where the first (R CPE) element corresponds to the grain boundary contribution to the spectrum with a capacitance value in the order of 10^{-9} F for both

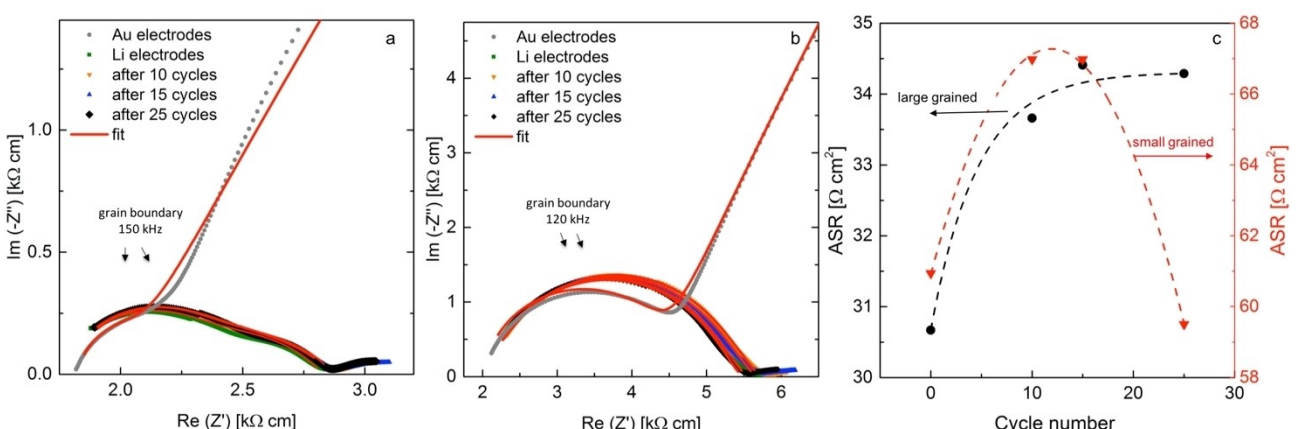


Figure 9. AC-impedance spectra at 298 K with blocking Au-electrodes and non-blocking Li-electrodes as-prepared and after cycling for ceramics with $x = 0.22$ with calcined (a), calcined then ball milled starting powder (b) and ASR values for large ($2.2 \mu\text{m}$) and small grained ($0.7 \mu\text{m}$) ceramics measured before and after cycling at different current densities (dashed lines act as visual aid only) (c).

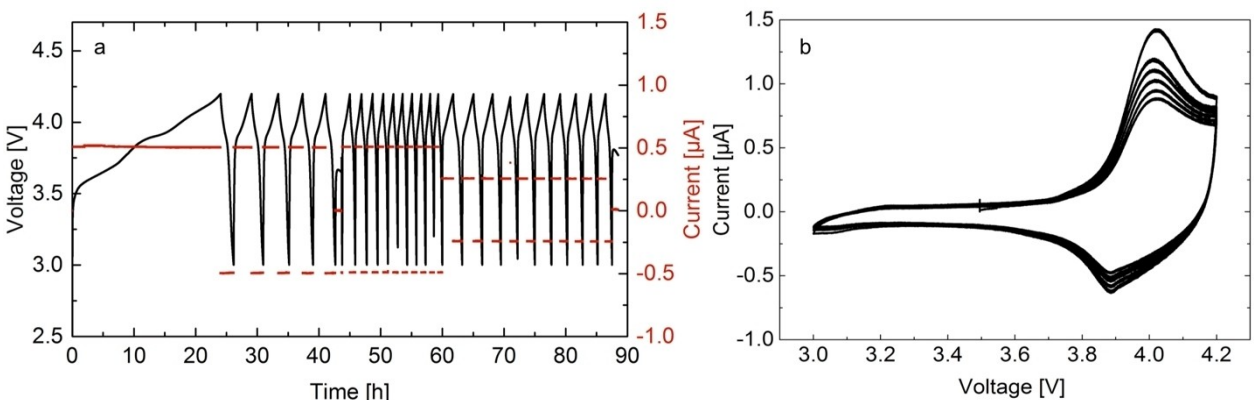


Figure 10. Galvanostatic cycling of LCO|LLZO|Li cells at 0.5 μ A and 0.25 μ A in the potential range between 3 V and 4.2 V vs. Li/Li⁺ for a total of 25 cycles at 25 °C (a), cyclic voltammograms between 3 and 4.2 V vs. Li⁺/Li with a cycling rate of 0.1 mVs⁻¹ obtained after cycling for 5 galvanostatic cycles (b).

samples, while the second (R CPE) element corresponds to the charge transfer for both electrodes and its capacitance calculates to 10^{-8} F for the large grained ceramic and 10^{-9} F for the small grained ceramic. The grain boundary resistance is fixed for all the fits to the value measured with blocking Au-electrodes.

The ASR values and their evolution after cycling are presented in Figure 9 c. The large grained ceramic has an ASR of $30.7 \Omega \text{cm}^2$ against Li metal, which is among the best values reported to date. The ASR value increases after cycling at $75 \mu\text{A cm}^{-2}$ reaching $34.4 \Omega \text{cm}^2$ and remains stable at $34.3 \Omega \text{cm}^2$ after additional cycling at $50 \mu\text{A cm}^{-2}$. The ASR for the small-grained ceramic are almost double compared to what was measured for the ceramic with a larger grain size. Before cycling the ASR is determined to $61 \Omega \text{cm}^2$, then it increases to $67 \Omega \text{cm}^2$ and remains stable even at the higher current density. After additional 10 cycles at the initial current density the ASR decreases to $59.5 \Omega \text{cm}^2$. This decrease is significant, and the authors assume that a small-grained ceramic might have an improved long term stability of the interface towards Li metal, but it definitely results in a higher ASR than the larger grained counterpart. Additional investigations are required for the interface between Li-metal and LLZO, where the ceramic surface would need to meet different requirements than the interior of the solid electrolyte. These requirements can be met for example through surface coatings, suppressing electric field inhomogeneity across the interface and thereby suppressing dendrite formation.

The large-grained ceramic showing superior electrochemical performance was utilized to assemble a full all-solid-state cell with a Li-metal anode and thin-film LiCoO₂ (LCO) cathode. The LCO thin-film deposition using laser assisted chemical vapor deposition (LA-CVD) has many advantages, most prominent is the good contact between the cathode and the solid electrolyte, due to the relatively high deposition temperature. Additionally, the LCO film is dense and it is phase pure.^[11] Furthermore, for thin-film LCO cathodes there is no need for the addition of an electronically conductive material, e.g., carbon black.^[25] Figure 10 shows the galvanostatic cycling and cyclic voltammetry results for the LCO|LLZO|Li cell. The first

charging step of the all-solid-state cell shows two plateaus; the first at 3.6 V and the second at 3.9 V vs. Li⁺/Li. The first plateau corresponds to a non-reversible reaction occurring at the interface between LCO and LLZO. It has to be noted, that Li₂CO₃ is formed during the cathode deposition as an intermediate product due to the reaction of the carbon containing Li precursor with oxygen gas.^[11] Since the deposition temperature is set to 700 °C Li₂CO₃ might have not completely decomposed, residing at the interface between LCO and LLZO. It is very likely that a non-reversible decomposition is taking place at the interface creating solid Li₂O and CO₂ gas, which might lead to a reaction with LiCoO₂ resulting in a compound with different redox potential, which we assigned to the irreversible plateau at 3.6 V. The second plateau at 3.9 V is expected and is related to the delithiation of the active material during the charging process.^[26] During the first discharge, the plateau at 3.9 V is reversible and stable, yet less pronounced throughout 25 cycles. After performing stable galvanostatic cycling for approximately 40 hours, cyclic voltammetry is performed. As it is shown in Figure 10b, the cell shows reversible cycling behavior for additional 5 cycles with a cycling rate of 0.1 mVs⁻¹ at 25 °C. An overpotential of 120 mV for the LCO|LLZO|Li cell is detected. Additionally, the current observed during the charging process is higher than the one observed during discharge. A possible reason for this asymmetry of the cyclic voltammograms is the reduced kinetics during lithiation of the cathode compared to its delithiation at the chosen cycling rate.

3. Conclusions

To determine the influence of the grain size on the electrochemical performance of $\text{Li}_{7-3x}\text{La}_3\text{Zr}_2\text{Al}_x\text{O}_{12}$ the compositional and structural differences of the grain boundaries of the large- and small-grained ceramics were eliminated. The approach of employing a single synthesis route for the large and small grained ceramics is a great advantage, as such differences can be minimized. In this study, a smaller grain size of 0.7 μ m leads to a significantly lower ionic conductivity across the entire temperature range, compared to a grain size of 2.2 μ m as well

as an increase of the activation energy. The separation of the bulk and grain boundary contributions confirms that the observed influence is due to the increased number of grain boundaries and not only due to the increased Li loss expected for ceramics with a finer starting powder. The activation energies for small and large grained ceramics are different, therefore, the Li-ion conductivity is dependent on the operating temperature of the cell assuming structural and compositional stability. Since the solid electrolyte is meant to be used mainly at room temperature, samples synthesized using the combination of NSP and FAST would have an optimal grain size of 2–3 µm, where the conductivity is double and the ASR is half of that of the counterpart with a grain size of 0.7 µm. An all-solid-state cell with the optimized LLZO ceramic electrolyte, a LCO cathode deposited using LA-CVD and Li-anode was cycled at room temperature.

Acknowledgements

M. Botros and H. Hahn acknowledge the German Research Foundation (DFG) for project no. SE 1407/4-2 and HA 1344/45-1 (424789449). O. Clemens acknowledges funding by DFG within CL551/3-1. This work was partly carried out with the support of the Karlsruhe Nano Micro Facility (KNMF, www.knmf.kit.edu), a Helmholtz Research Infrastructure at Karlsruhe Institute of Technology. We acknowledge support by the KIT-Publication Fund of the Karlsruhe Institute of Technology. Open Access funding enabled and organized by Projekt DEAL.

Conflict of Interests

The authors declare no conflict of interest.

Data Availability Statement

The data that support the findings of this study are available from the corresponding author upon reasonable request.

Keywords: Garnet solid electrolyte • conductivity • microstructure • field assisted sintering • all-solid-state battery

- [1] L. Cheng, W. Chen, M. Kunz, K. Persson, N. Tamura, G. Chen, M. Doeff, *ACS Appl. Mater. Interfaces* **2015**, *7*, 2073.
- [2] M. Ashuri, M. Golmohammad, A. Soleimany Mehranjani, M. Faghihi Sani, *J. Mater. Sci. Mater. Electron.* **2021**, *32*, 6369.
- [3] J. Sastre, T. Y. Lin, A. N. Filippin, A. Priebe, E. Avancini, J. Michler, A. N. Tiwari, Y. E. Romanuk, S. Buecheler, *ACS Appl. Energ. Mater.* **2019**, *2*, 8511.
- [4] Y. Ren, Y. Shen, Y. Lin, C.-W. Nan, *ACS Appl. Mater. Interfaces* **2019**, *11*, 5928.
- [5] J. Sakamoto, E. Rangasamy, H. Kim, Y. Kim, J. Wolfenstine, *Nanotechnology* **2013**, *24*, 424005.
- [6] F. Monteverde, *J. Alloys Compd.* **2007**, *428*, 197.
- [7] R. Djenadic, M. Botros, C. Benel, O. Clemens, S. Indris, A. Choudhary, T. Bergfeldt, H. Hahn, *Solid State Ionics* **2014**, *263*, 49.
- [8] A. Paoletta, W. Zhu, G. Bertoni, S. Savoie, Z. Feng, H. Demers, V. Gariepy, G. Girard, E. Rivard, N. Delaporte, A. Guerfi, H. Lorrmann, C. George, K. Zaghib, *ACS Appl. Energ. Mater.* **2020**, *3*, 3415.
- [9] S. Filipović, N. Obradović, V. B. Pavlović, M. Mitrić, A. Đorđević, M. Kachlik, K. Maca, *IEEE Trans. Ind. Electron.* **2016**, *42*, 9887.
- [10] M. Winterer, V. V. Srdic, R. Djenadic, A. Kompch, T. E. Weirich, *Rev. Sci. Instrum.* **2007**, *78*, 123903. DOI 10.1063/1.2821234.
- [11] C. Loho, A. J. Darbandi, R. Djenadic, O. Clemens, H. Hahn, *Chem. Vap. Deposition* **2014**, *20*, 152.
- [12] M. Botros, R. Djenadic, O. Clemens, M. Matthias, H. Hahn, M. Möller, H. Hahn, *J. Power Sources* **2016**, *309*, 108.
- [13] R. A. Young, *The Rietveld Method*, International Union Of Crystallography, Oxford University Press, **1993**.
- [14] B. H. Toby, *Powder Diffraction* **2006**, *21*, 67.
- [15] F. Lin, I. M. Markus, M. M. Doeff, H. L. Xin, *Sci. Rep.* **2014**, *4*, 1.
- [16] M. Botros, T. Scherer, R. Popescu, A. Kilmametov, O. Clemens, H. Hahn, *RSC Adv.* **2019**, *9*, 31102.
- [17] M. M. Ahmad, *RSC Adv.* **2015**, *5*, 25824.
- [18] R. P. Rao, W. Gu, N. Sharma, V. K. Peterson, M. Avdeev, S. Adams, *Chem. Mater.* **2015**, *27*, 2903.
- [19] A. Kilmametov, R. Gröger, H. Hahn, T. Schimmel, S. Walheim, *Adv. Mater. Technol.* **2016**, 1600115.
- [20] A. Moradabadi, P. Kaghazchi, *Solid State Ionics* **2019**, *338*, 74.
- [21] D. Wang, G. Zhong, O. Dolotko, Y. Li, M. J. McDonald, J. Mi, R. Fu, Y. Yang, *J. Mater. Chem. A* **2014**, *2*, 20271.
- [22] M. Sotoudeh, S. Baumgart, M. Dillenz, J. Döhn, K. Forster-Tonigold, K. Helmbrecht, D. Stottmeister, A. Groß, *Adv. Energy Mater.* **2023**, *2302550*.
- [23] T. Famprakis, P. Canepa, J. A. Dawson, M. S. Islam, C. Masquelier, *Nat. Mater.* **2019**, *18*, 1278.
- [24] F. M. Pesci, A. Bertei, R. H. Brugge, S. P. Emge, A. K. O. Hekselman, L. E. Marbella, C. P. Grey, A. Aguadero, *ACS Appl. Mater. Interfaces* **2020**, *12*, 32806.
- [25] H. Xia, Y. S. Meng, L. Lu, G. Ceder, S. Alliance, *Sci. Commons* **2010**.
- [26] E. Antolini, *Solid State Ionics* **2004**, *170*, 159.

Manuscript received: April 26, 2024
Accepted manuscript online: May 2, 2024
Version of record online: June 25, 2024